RESEARCH PAPER

SPECIAL SERIES ON MITOCHONDRIAL BIOENERGETICS IN PHYSIOLOGY

Comparative functional analysis reveals differential nucleotide sensitivity between human and mouse UCP1

Eva Musiol[1] | Tobias Fromme[1,2] | Julia Hau[1] | Antonella Di Pizio[3,4] | Martin Klingenspor[1,2]

[1]Chair for Molecular Nutritional Medicine, TUM School of Life Sciences, Research Department of Molecular Life Sciences, Technical University of Munich, Freising, Germany

[2]EKFZ—Else Kröner Fresenius Center for Nutritional Medicine, Technical University of Munich, Munich, Germany

[3]Molecular Modeling Group, Leibniz Institute for Food Systems Biology at the Technical University of Munich, Freising, Germany

[4]Professorship of Chemoinformatics and Protein Modelling, TUM School of Life Sciences, Research Department of Molecular Life Sciences, Technical University of Munich, Freising, Germany

Correspondence

Martin Klingenspor, Chair for Molecular Nutritional Medicine, TUM School of Life Sciences, Research Department of Molecular Life Sciences, Technical University of Munich, Freising, Germany.
Email: mk@tum.de

Abstract

Aim: Mitochondrial uncoupling protein 1 (UCP1) is a unique protein of brown adipose tissue. Upon activation by free fatty acids, UCP1 facilitates a thermogenic net proton flux across the mitochondrial inner membrane. Non-complexed purine nucleotides inhibit this fatty acid-induced activity of UCP1. The most available data have been generated from rodent model systems. In light of its role as a putative pharmacological target for treating metabolic disease, in-depth analyses of human UCP1 activity, regulation, and structural features are essential.

Methods: In the present study, we established a doxycycline-regulated cell model with inducible human or murine UCP1 expression and conducted functional studies using respirometry comparing wild-type and mutant variants of human UCP1.

Results: We demonstrate that human and mouse UCP1 exhibit similar specific fatty acid-induced activity but a different inhibitory potential of purine nucleotides. Mutagenesis of non-conserved residues in human UCP1 revealed structural components in α-helix 56 and α-helix 6 crucial for uncoupling function.

Conclusion: Comparative studies of human UCP1 with other orthologs can provide new insights into the structure–function relationship for this mitochondrial carrier and will be instrumental in searching for new activators.

KEYWORDS

brown adipose tissue, fatty acids, mitochondrial carriers, mutagenesis, proton leak, purine nucleotides, thermogenesis, uncoupling proteins

1 | INTRODUCTION

Non-shivering thermogenesis is a unique function of mammalian brown adipose tissue (BAT) and the uncoupling protein 1 (UCP1). Upon beta-adrenergic stimulation, long-chain fatty acids (LCFA) released by lipolysis activate the innately inactive UCP1, resulting in a proton-short circuit of the mitochondrial membrane potential, thus generating heat. The importance of BAT thermogenesis in small mammals has long been recognized. However, most of our understanding of BAT and UCP1 activity and regulation has been derived from studies of the rodent protein.

More than 15 years ago, functional BAT with beneficial metabolic outcomes was discovered in adult humans.[1–3] A large clinical study meanwhile underlined the cardiometabolic risks associated with low BAT activity.[4] Direct activators of UCP1 would circumvent detrimental side effects of sympathomimetics or other mediators of BAT thermogenesis. A deeper understanding of the structure–function relationship for human UCP1 (hUCP1) will assist in identifying such activators.

As a member of the mitochondrial solute carrier family 25 (*SLC25*), UCP1 comprises six α-helices with a threefold pseudosymmetry.[5] The binding of non-complexed purine nucleotides inhibits UCP1-dependent proton leak activity while LCFA override this inhibition.[6] Four biochemical models have been suggested for how LCFA activate UCP1-dependent proton translocation. In the allosteric model, binding of LCFA to UCP1 causes structural changes that open a proton transport channel across the inner mitochondrial membrane.[7,8] In the cofactor model, the carboxyl groups of LCFA bound to UCP1 complement an array of charged amino acid residues in the channel to enable proton translocation.[9] In the cycling model, proton transport results from UCP1 facilitating the flip-flop of negatively charged free LCFA anions back to the outer side of the inner mitochondrial membrane.[10] Finally, the symporter model suggests that LCFA bound to UCP1 by hydrophobic interaction enables proton transport, though LCFA/H$^+$ stoichiometry has not been investigated.[11]

To understand the structure–function relationship for mitochondrial carriers, including UCP1, the ADP/ATP carrier analyses served as a blueprint.[12] Initially, all mitochondrial carriers were thought to operate as dimers. Still, data from studies of the ADP/ATP carrier led to the insight that most mitochondrial carriers operate as monomers, including UCP1.[13,14] Analyses of the potential substrate binding sites established that all mitochondrial carriers bind their respective substrates at an internal cavity of the carrier,[12] as demonstrated for the ADP/ATP carrier.[15] Resolution of the matrix-open state (m-state) of the ADP/ATP carrier revealed that fluctuations from the cytoplasmic-open state (c-state) to the m-state of the central cavity catalyzes transport.[16,17] The carrier motif, which stabilizes the c-state of ADP/ATP carrier, is present in all members of the mitochondrial carrier family, including UCP1.[17–19]

Before the recent resolution of the UCP1 structure by cryo-electron microscopy,[20,21] several studies applied mutagenesis to gain insights into structure–function relationships. Early on, conserved residues in α-helix 6 were suggested to be involved in purine nucleotide binding using photoaffinity labeling methods.[22,23] Deletion of three amino acids in this region (F268/K269/G270) completely abrogated guanosine-di-phosphate (GDP)

inhibition of proton leak.[24] However, further mutagenesis experiments provided evidence for a more complex interaction network conveying purine nucleotide binding in the tripartite structure, as exemplified by the requirement of R84, R183, and R277 for purine nucleotide binding[25] and the potential role of E191 in pH-dependent affinity.[26] Among several other residues interacting with GDP, simulations of intramolecular contacts suggest R277 and L278 contacting the phosphate moiety and W281 forming hydrophobic interaction with the purine base.[27] These residues are located on α-helix 6 close to the hinge region between α-helix 56 and α-helix 6. Recent reports on the hUCP1 structure elucidated by cryo-electron microscopy now consolidated how the core interaction network binds the purine nucleotide molecule in the internal cavity of the channel, also showing the participation of residues on α-helix 6 in purine nucleotide binding, namely hydrogen bonds of R277 with γ-phosphate of GTP and N282 with guanine.[20,21] The binding of GTP or ATP prevents proton translocation by stabilizing UCP1 in a conformation resembling the c-state of the ADP/ATP carrier in the presence of carboxy-atractyloside.[15] In this conformation, a matrix insulator is formed, which blocks the transit of protons.[20,21] The availability of UCP1 structures has set the stage for elucidating the allosteric mechanisms involved in purine nucleotide binding and LCFA-dependent activation of proton transport.

Most functional studies were performed with rodent UCP1 in either isolated yeast mitochondria or proteoliposomes, potentially limiting the functionality of UCP1 (reviewed in[28]). Studies on hUCP1, however, are rare.[20,21,29,30] The primary structures of hUCP1 and mUCP1 share 79% and 89% sequence identity and similarity, respectively. A comparison of these orthologs expressed in yeast observed no basal proton conductance of hUCP1, along with less GDP sensitivity of palmitate-induced respiration.[30] In contrast, human BAT was reported to be sensitive to GDP.[31] More studies directly comparing rodent and human UCP1 orthologs are needed to enable translational insights. While the role of BAT in rodents and its link to obesity is well established, the relevance of human BAT in the context of metabolic diseases can be questioned.[32] Regarding the far lower amounts of BAT in relation to whole body weight, it is a matter of debate whether therapeutic stimulation of BAT would cause a substantial increase in total energy expenditure.[33,34]

Here, we aim to determine whether hUCP1 and mUCP1 show similar activity, capacity, and regulation. This is one essential prerequisite to estimating the efficacy of potential therapies that stimulate human BAT thermogenesis for treating metabolic diseases. Hence, we established a doxycycline-regulated HEK cell model with inducible human or murine UCP1 expression. This model

enables the direct comparison of UCP1 function in a mammalian background. Using this method, we could establish that, despite a sequence identity of 79%, hUCP1 and mUCP1 exhibit similar specific fatty acid-induced activity but divergent inhibitory potential of purine nucleotides. Subsequent site-directed mutagenesis of non-conserved residues in α-helix 56 and α-helix 6 revealed structural features of hUCP1 essential for fatty acid-induced activation.

2 | RESULTS

We created a HEK-293 cell model with doxycycline-inducible UCP1 expression. This model system allows the investigation of UCP1 orthologs expressed in adjustable and comparable amounts. We first constructed six different cell lines expressing wild-type (WT) or tagged (C-FLAG, N-FLAG) versions of hUCP1 or mouse UCP1 (mUCP1). Before functional characterization, we conducted several tests to evaluate doxycycline-induced ectopic expression of tagged mUCP1 and hUCP1. Based on the adverse effects of doxycycline on mitochondrial function and protein homeostasis, we treated cells for 3 days at a concentration of 2.5 ng/mL doxycycline, which is two orders of magnitude below minimal detrimental concentrations.[35] Induction of ectopic expression of either tagged mUCP1 or hUCP1 with doxycycline did not impair cell growth compared to the untreated controls (+Dox vs. −Dox in Figure S1A,B). For hUCP1, the growth rate was also similar for N-FLAG and C-FLAG (Figure S1A), while for mUCP1, C-FLAG showed less growth compared to N-FLAG (Figure S1B). FLAG-tagged mUCP1 and hUCP1 were localized in mitochondria, as demonstrated by the co-staining of HSP60 (Figure S2A).

Basal leak respiration of permeabilized cells expressing either WT or FLAG-tagged UCP1 was comparable after adding pyruvate, malate, and succinate (Figure S1C,D). To exclude partial activation of UCP1 by low concentrations of free fatty acids in medium or cells, we demonstrate that buffering free fatty acids with BSA did not decrease basal leak respiration. Comparable basal leak respiration for cells expressing FLAG-tagged and WT UCP1 excludes innate constitutive uncoupling activity of FLAG-tagged UCP1 (Figure S3C,D). However, adding palmitic acid induced a more than six to eightfold increase in leak respiration rates in cells expressing WT and tagged UCP1 but not in control cells (Figure S1E–H). Notably, the lower growth of C-FLAG mUCP1-expressing cells did not affect respiration rates.

To further corroborate that doxycycline had no general effect on cell metabolism, we measured glucose depletion of the medium over time (Figure S3A,B). Doxycycline-treated cells expressing UCP1 and control cells without

UCP1, 3 and 24 h after provision of fresh medium, showed a similar glucose clearance of ~10% and ~50%, respectively (Figure S3A,B). Adding palmitic acid as an activator of UCP1 to doxycycline-treated cells significantly increased glucose clearance to ~25% and 75%, respectively (Figure S3A,B). This aligns well with the more than six-fold increase in palmitate-induced respiration rates in these cells (Figure S1G,H). Glucose clearance in response to palmitate was not tested in control cells but is unlikely to increase as there was no effect of palmitate on respiration in these cells (Figure S1G,H).

Taken together with a doxycycline-induced expression of FLAG-tagged UCP1 in HEK298 cells, we observed average cell growth, mitochondrial localization of ectopically expressed UCP1 and fatty acid-induced leak respiration. The FLP-mediated recombination ensures site-specific integration of the target gene into the identical genomic locus,[36] and the human CMV promoter warrants high UCP1 expression levels. Adding FLAG-tags to UCP1 orthologs facilitates exact quantitation without affecting respiration rates and, thus, on UCP1 function (Figure S1E–H). Leak respiration, substrate leak respiration, and palmitate-induced leak respiration were comparable between tagged and untagged versions of hUCP1 and mUCP1. As a result, we conclude that the established cell system with ectopically expressed FLAG-tagged UCP1 is suitable for conducting comparative functional studies of UCP1 orthologs and mutant variants.

2.1 | Activation of UCP1 orthologs by long-chain free fatty acids

Using the inducible HEK298 cell system, we determined whether hUCP1 and mUCP1 share similar activity, capacity, and regulation. LCFA are natural activators of UCP1. We tested fatty acid-mediated activation of hUCP1 and mUCP1 in trypsinized, permeabilized HEK293 cells through palmitic acid titration. In the absence of palmitate, expression of innately inactive hUCP1 and mUCP1 did not elevate basal proton leak (Figure 1A). In the presence of 517 nM palmitate, UCP1-mediated proton leak was of proportionate magnitude in the mouse and human orthologs (Figure 1B), leading to a more than threefold increase above basal proton leak respiration at comparable absolute UCP1 protein abundance per cell (Figure 1B,C). The titration of palmitic acid evoked similar kinetic responses of hUCP1 and mUCP1 mediated proton leak. Both hUCP1 and mUCP1 displayed a similar dose-dependent activation by palmitate (Figure 1D,E) with similar half-maximal activation constants (Figure 1F). The known unspecific uncoupling effect of free fatty acids was excluded through a control experiment. Two orders of magnitude
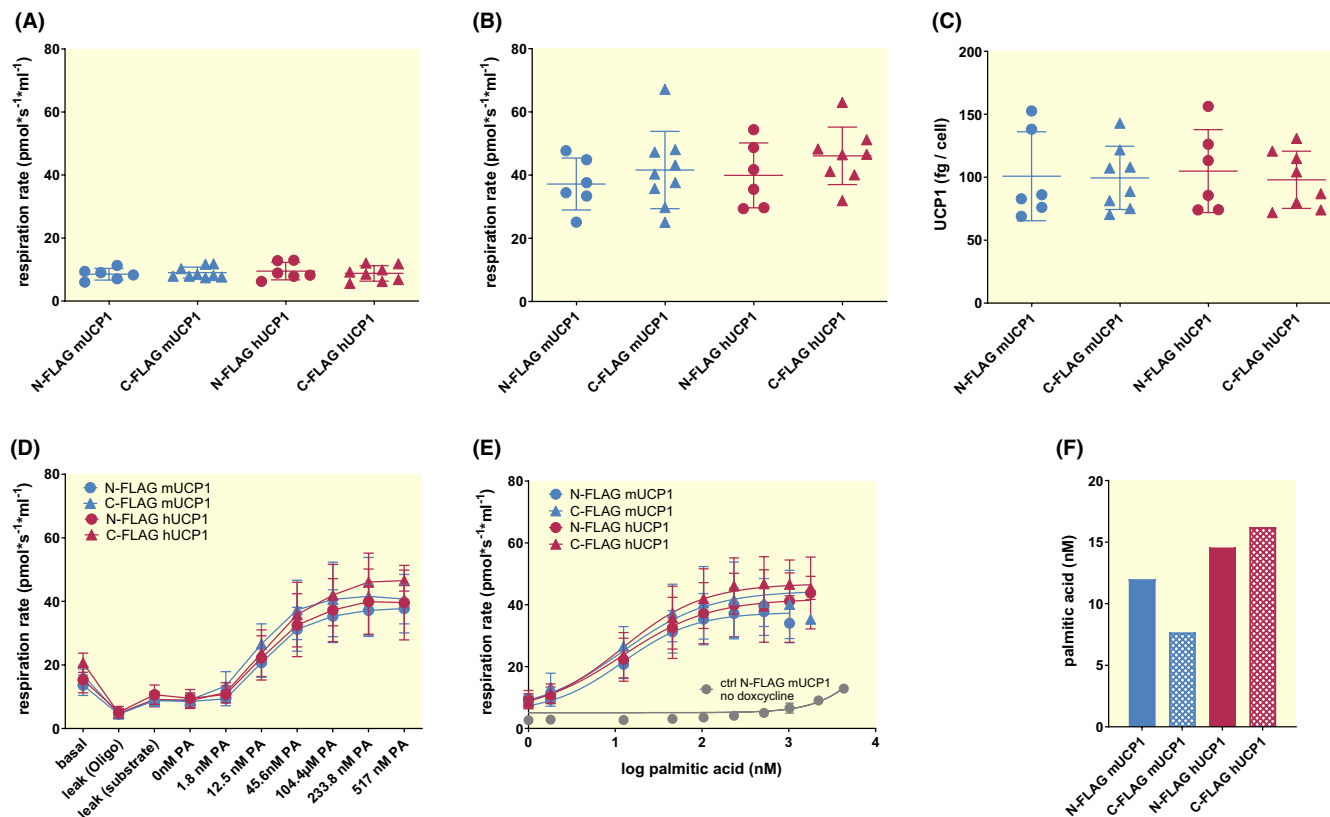
FIGURE 1 Palmitate-induced activation of ectopically expressed UCP1 in HEK293 cells. Respirometry measurements were performed for human and murine UCP1 tagged with a FLAG-tag on either the N- or C-terminus. (A) Leak respiration rates in the absence of palmitic acid [0 nM]. (B) Palmitate-induced leak respiration, [517 nM] free palmitate. (C) Amount of UCP1 per cell in each high-resolution respirometry sample; determination was done with a recombinant N-FLAG-mUCP1 standard on a Western Blot; one-way ANOVA revealed no significance for data in A, B, and C ($p > 0.05$). (D) Respiration rates during palmitate titration assay. (E) Dose–response curves for palmitate calculated through a least square regression assuming a four-parameter sigmoidal relationship to log[palmitate] with a fixed bottom respiration value; gray circles = control (non-induced HEK293 cells); All data as mean $\pm$ SD, $n = 6$–9. (F) EC50 values for half-maximal palmitate-induced respiration, derived from the dose–response curves in (E), showed no significant difference between cell lines ($p = 0.2374$). Comparison of EC50 in the fitted models was performed by an extra sum-of-square F test.

higher concentrations of palmitic acid were needed to induce an unspecific proton leak in control cells not expressing UCP1 (Figure 1E). The observed palmitate-mediated UCP1 activity in induced HEK293 cells is thus wholly attributable to the ectopically expressed UCP1.

2.2 | Purine nucleotide sensitivity differs between human and mouse UCP1

Free fatty acids activate UCP1 while binding of non-complexed purine nucleotides to UCP1 inhibits proton leak. Purine tri- and di-phosphate nucleotides show slightly different affinities for purified UCP1 in the low micromolar range, with ADP showing the least affinity with the highest dissociation constant (GTP < GDP < ATP < ADP).[37] However, the pool size of adenosine phosphate nucleotides in BAT is way larger compared to guanosine.[38] Through respirometry, we investigated differences in purine nucleotide

sensitivity between hUCP1 and mUCP1 in trypsinized, induced HEK293 cells (Figure 2A). Again, in the absence of fatty acids, basal leak respiration rates were similar in cells expressing mouse and hUCP1, and UCP1-mediated proton leak respiration was equally activated through a set dose of palmitate (79 nM) with both orthologs (Figure 2B).

A stepwise increase in ADP concentrations (0.25–10 mM) resulted in efficient inhibition of hUCP1 and mUCP1, which showed similar dose-dependent kinetics (Figure 2C). The correlative half-maximal inhibitor constants (IC50) of hUCP1 thus matched the mUCP1 IC50 (Figure 2D).

In a comparative assessment of GDP inhibition (Figure 3A), palmitate-evoked activation (Figure 3B) of hUCP1 and mUCP1 was inhibited through GDP titration (Figure 3C). While mUCP1 decreased activity upon the lowest GDP dosage (0.25 mM), hUCP1 showed varying sensitivity. The dynamic range of GDP inhibition was significantly more extensive for mUCP1 compared to hUCP1. Even at
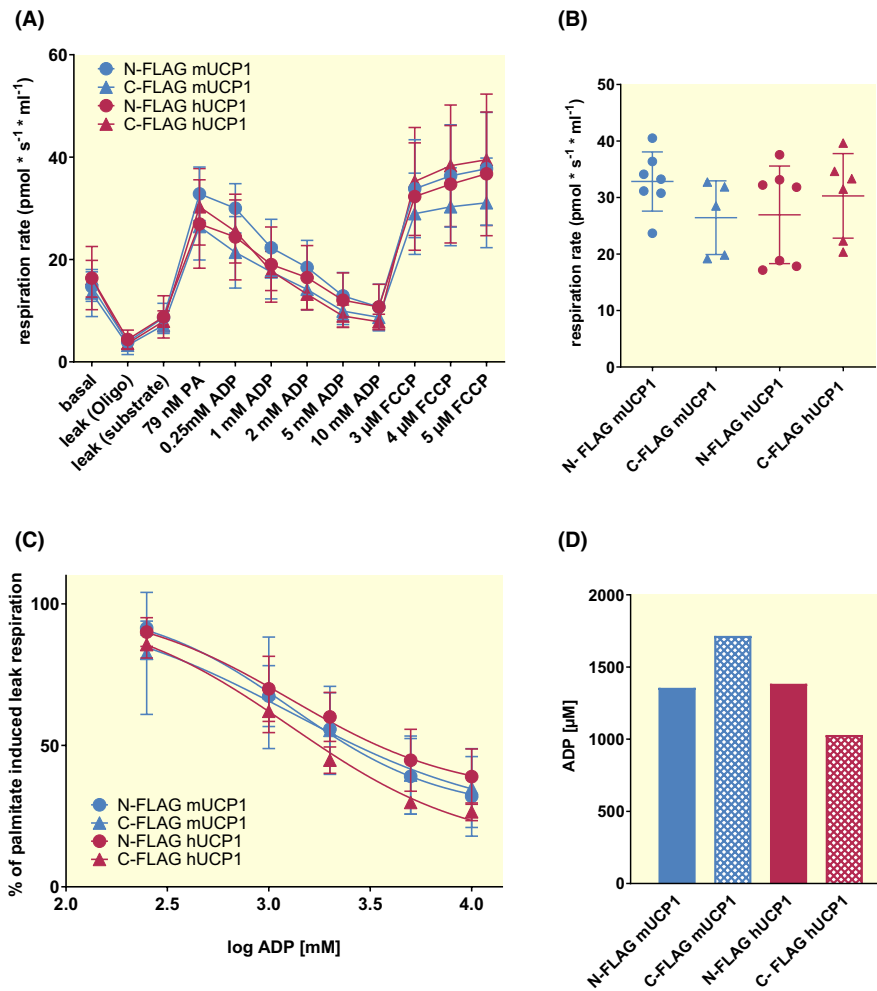
FIGURE 2 ADP titration of induced HEK293 cells. Respirometry measurements were performed with cells expressing human or murine UCP1 tagged with a FLAG-tag on either the N- or C-terminus of the protein. (A) Respiration rates during ADP-titration assay. After basal respiration was recorded, oligomycin was applied to inhibit the ATPase. Subsequently, cells were permeabilized with α-chaconine and supplied with substrates (pyruvate, malate, and succinate); UCP1 was activated through a set dose of palmitate (79 nM) followed by stepwise inhibition of UCP1 through ADP (0.25–10 mM). Finally, FCCP was applied to fully uncouple mitochondrial respiration. (B) Palmitate-induced proton leak [79 nM] free palmitate; One-way ANOVA $p > 0.05$. (C) Dose–response curves for the inhibition of proton leak respiration by ADP after normalizing to maximal palmitate-induced proton leak; all data as mean $\pm$ SD, $n = 5$–7. Curves were calculated through a least square regression assuming a four-parameter sigmoidal relationship to log[ADP] with a fixed top respiration value. Comparison of half-maximal ADP doses (IC50) of fitted models was performed by an extra sum-of-square F test. (D) IC50 values for ADP, derived from the dose–response curves in (C), were not significantly different ($p = 0.9094$).

the highest GDP concentrations (10 mM), hUCP1 displayed higher proton leak than mUCP1 (Figure 3C), resulting in a more than 14-fold higher half-maximal IC50 for N-FLAG hUCP1 compared to N-FLAG mUCP1 (Figure 3D).

2.3 | Amino acids in α-helix 56 and α-helix 6 are essential for the functionality of UCP1

To explore the distribution of diverse amino acids between mUCP1 and hUCP1, we mapped these positions on the 3D structure of hUCP1 (PDB ID: 8G8W; Figure 4).[20]

Human-mouse sequence differences are more abundant in extra-bilayer regions of UCP1 than in intra-bilayer regions, of which nine amino acid differences are found in α-helix 56 and N-terminal α-helix 6, located in the matrix gate and matrix insulator area. We hypothesized that these residues could increase GDP sensitivity by facilitating allosteric conformational changes induced by the purine nucleotide binding in the central cavity.

Through the site-directed introduction of mouse amino acids, we aimed to generate a variant hUCP1 with unchanged fatty acid-induced activation but increased, that is, mouse-like, GDP sensitivity. We thus generated nine mutant N-FLAG hUCP1 cell lines by replacing the
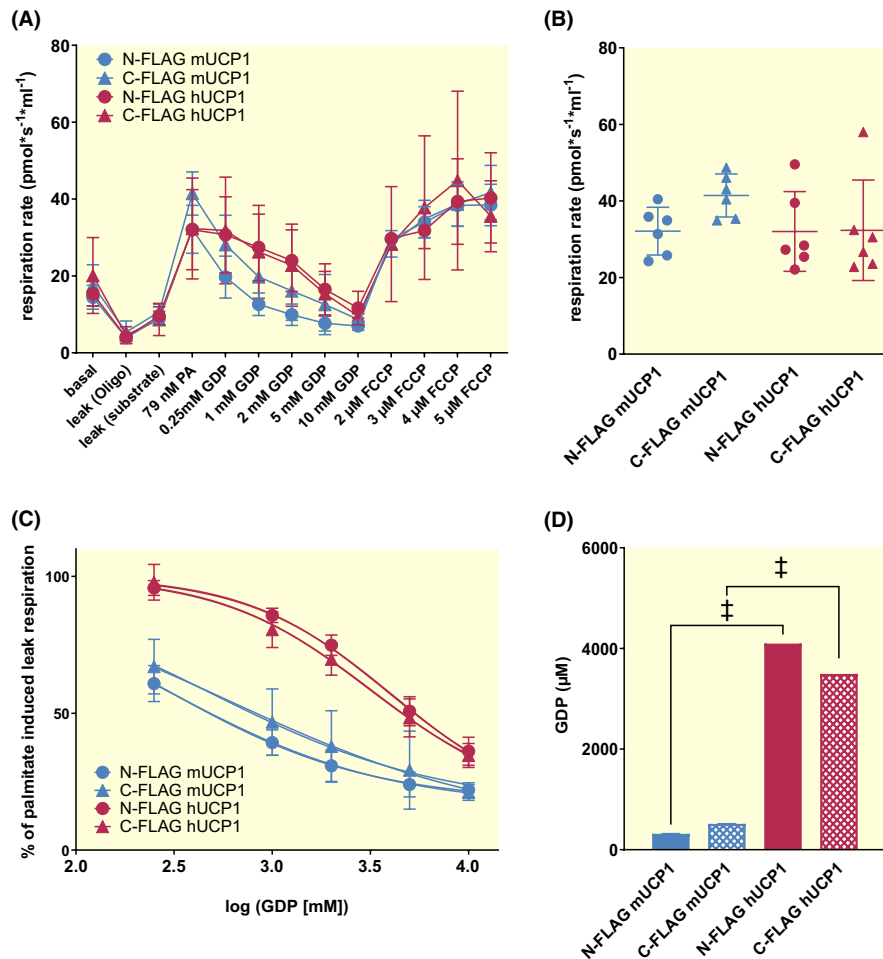
FIGURE 3 GDP titration measurements of induced HEK-293 cells. High-resolution respirometry measurements were performed with cells expressing human or murine UCP1 tagged with a FLAG-tag on either the N- or C-terminus of the protein. (A) Respiration rates during GDP-titration assay. After basal respiration was recorded, oligomycin was applied to inhibit the ATPase. Subsequently, cells were permeabilized with α-chaconine and supplied with substrates (pyruvate, malate, and succinate); UCP1 was activated through a set dose of palmitate [79 nM] followed by the stepwise inhibition of proton leak through GDP [0.25–10 mM]. FCCP was applied to fully uncouple mitochondrial respiration. (B) Palmitate-induced proton leak [79 nM]. (C) Dose–response curve for the inhibition of proton leak respiration by GDP after normalizing to maximal palmitate-induced proton leak; all data as mean ± SD, $n = 6$; dose–response curves in (C) were calculated through a least square regression assuming a four-parameter sigmoidal relationship to log[ADP] with a fixed top respiration value. Comparison of half-maximal GDP doses (IC50) of fitted models was performed by an extra sum-of-square F test. (D) IC50 values for GDP, derived from the curves in (C), were significantly different as indicated by asterisks (‡, $p < 0.001$).

corresponding amino acid in hUCP1 with the murine variant (Figure 5; Table S4).

Functional characterization of the UCP1 mutants by respirometry revealed that none of the nine introduced mutations in hUCP1 led to a similar GDP sensitivity as mUCP1 (Figure 5). The dose–response of all these could be fitted to relationships with the same half-maximal inhibition constants. In contrast, mUCP1 could not (nonlinear four-factor sigmoidal curve fit with Extra sum-of-squares F test comparing each fit to IC50 of hUCP1). However, five amino acid exchanges (K257S, V258M, N261K, L271F, and P273A) interfered with hUCP1 activity (Figure 5). Applying an initial palmitate bolus activated proton leak respiration to a much lower degree compared to wild-type hUCP1.

We further studied this unexpected phenomenon by palmitate titration (Figure S4). For the five mutations (K257S, V258M, N261K, L271F, and P273A), the dose–response relationship could indeed not be described by a sigmoidal fit of the same half-maximal palmitate dose and the same maximal induced respiration as the wild-type hUCP1 (Table S5). However, the trend toward higher EC50 values for four of the variants was not consolidated when fitting selectively for EC50 (Table S5). We, therefore, evaluated the potential effects on the half-maximal activating palmitate concentration (EC50) by fitting the relative palmitate-induced activation as a percentage of the maximal respiration for each replicate. The EC50 value for palmitate was increased for the
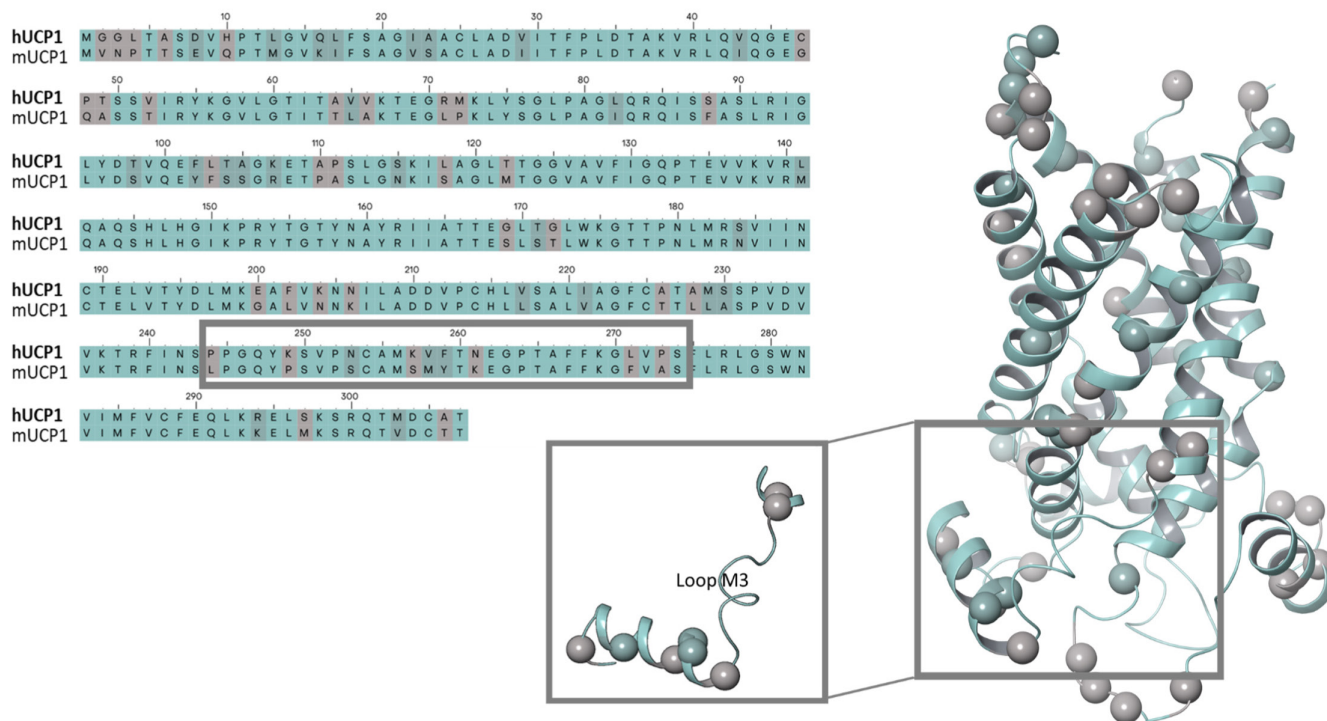
FIGURE 4 Structural features of hUCP1 and mUCP1. Left: Sequence alignment of hUCP1 (ENST00000262999.4) and mUCP1 (ENSMUST00000034146.5). Sequence identity and similarity of the orthologs are 79% and 89%, respectively; Right: 3D representation of UCP1 structure (8G8W.pdb); orbs represent the variant residues of the two orthologs. The same color scheme is used for both representations cyan: Cyan = identical residue, dark cyan = similar residues, dark gray = dissimilar residues.

P273A as compared to hUCP1, indicating reduced fatty acid sensitivity in this variant (Figure S5).

Mapping all nine exchanges to the 3D model, we found that the first seven amino acids (P244, K249, N253, K257, V258, F259, and N261) are located on the α-helix 56, while the other two amino acids (L271 and P273) are situated at the matrix terminus of α-helix 6. To shed light on the significance of these secondary structural features, we entirely replaced these two seemingly independent building blocks, resulting in the creation of two novel cell lines (Figure 6A; green orbs = N-FLAG hUCP1-N- terminal-7, blue orbs = N-FLAG hUCP1-C-terminal-2).

Within the two sets (N-terminal-7 and C-terminal-2), amino acid replacements interacted with each other in unique ways. The seven amino acid changes collectively located on α-helix 56 (Figure 6A) entirely complemented their individual effects (Figure 6B). The dose-dependent response of this construct could be described by a model with the same half-maximal palmitate concentration and maximal induced respiration rate as wild-type hUCP1 (Table S5). The EC50 for relative palmitate-induced activation of N-terminal-7 was similar to hUCP1 controls (Figure S5). In other words, the complete mouse version of α-helix 56 was as functional as the human version. In contrast, three single amino acid exchanges within α-helix 56 (K257S, V258M, and N261K) appear to impact activity

(see Figure 5D,E,G), identifying this small α-helix as a critical structural component of UCP1.

The two amino acid exchanges in α-helix 6 did not at all complement each other but conversely displayed an additive effect entirely abrogating any UCP1 activity (Figure 6C). This variant, N-FLAG hUCP1-C-terminal-2, led to markedly lower UCP1 protein levels in the doxycycline-induced cells (approximately one-third compared to wild-type and other variants), albeit with correct mitochondrial subcellular localization (Figure S2). While the absolute magnitude of fatty acid-induced respiration is thus debatable in this construct, the two murine amino acids did not compensate for each other's effect. Their loss-of-function demonstrates the vital importance of this short hinge region connecting α-helix 56 and α-helix 6. This is further supported by the significant increase in EC50 for the relative palmitate-induced activation in P273A and N-terminal-2 as compared to hUCP1 (Figure S5).

Data are available at mediaTUM (https://doi.org/10.14459/2024mp1740589).

3 | DISCUSSION

Mammalian UCP1 is a unique BAT mitochondria protein. Functional data on hUCP1, however, are scarce.
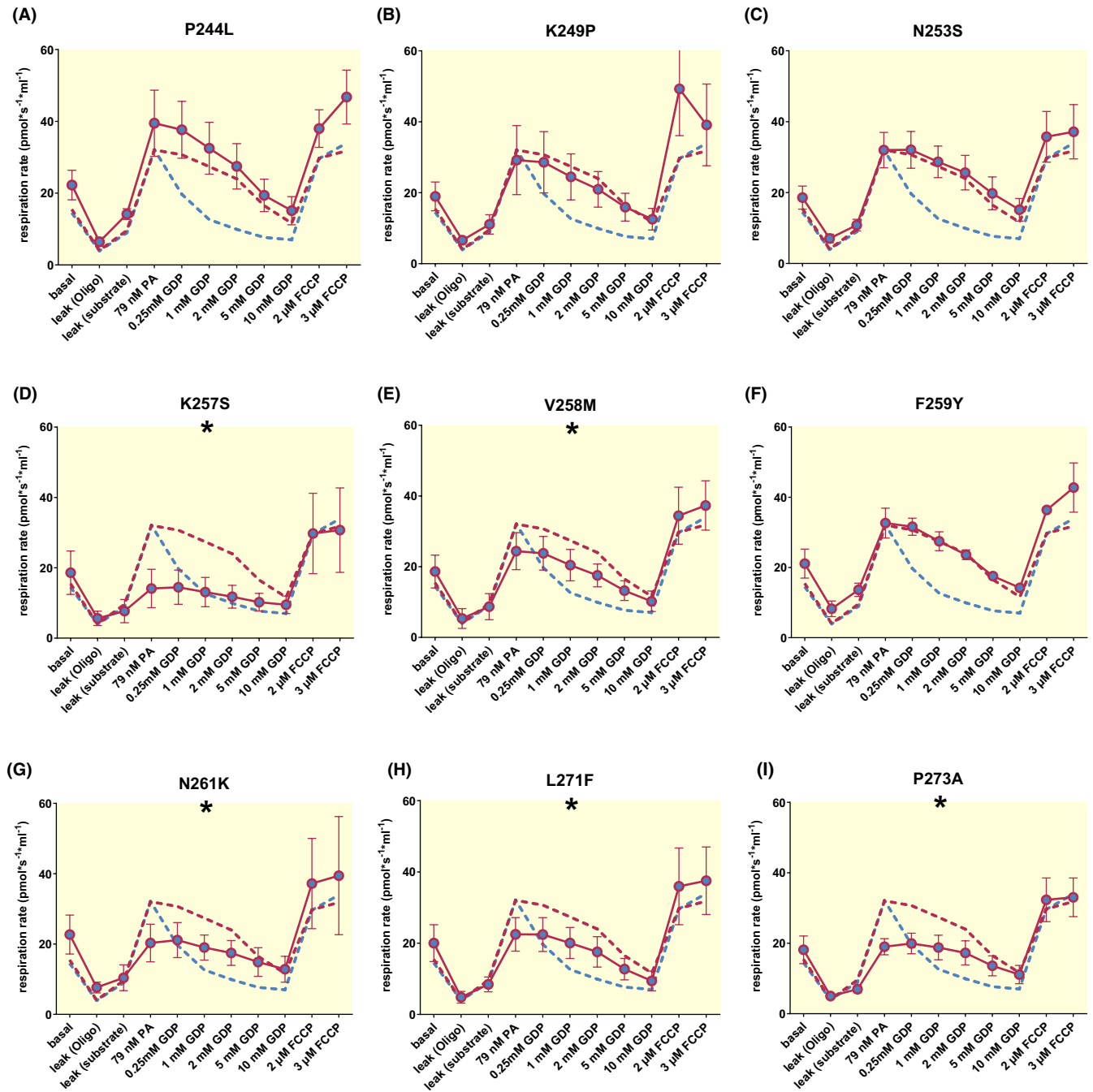
FIGURE 5 Influence of single amino acid exchange on the regulative capacity of GDP. GDP titration measurements of induced HEK293 cells expressing a variant N-FLAG hUCP1 (red lines with symbols) as compared to wild-type N-FLAG hUCP1 (dashed red line) and N-FLAG mUCP1 (dashed blue line). After basal respiration was recorded, oligomycin was applied to inhibit ATP synthase. Cells were permeabilized with α-chaconine and supplied with substrates (pyruvate, malate, and succinate); UCP1 activity was activated through a set dose of palmitate [79 nM] followed by the stepwise inhibition of proton leak through GDP (0.25 mM–10 mM). FCCP was applied to fully uncouple mitochondrial respiration. (A) N-FLAG hUCP1–P244L. (B) N-FLAG hUCP1—K249P. (C) N-FLAG hUCP1—N253S. (D) N-FLAG hUCP1—K257S. (E) N-FLAG hUCP1—V258M. (F) N-FLAG hUCP1—F259Y. (G) N-FLAG hUCP1—N261K. (H) N-FLAG hUCP1—L271F. (I) N-FLAG hUCP1—P273A. All data as mean ± SD, $n = 5$–7. Mutants labeled with asterisks showed different dose–response curves of palmitate-induced respiration (Figure S4). Statistics are shown in Table S5.

Our knowledge of function, regulation, and sensitivity toward its regulators stems from studies of the rodent protein. Thus, a thorough understanding of the comparative functionality of these UCP1 orthologs is essential to extrapolate the efficacy of putative drugs targeting human BAT thermogenesis for treating metabolic disease (reviewed in[39]). It is vital to comprehend not only the mechanisms that regulate the activity of BAT or lead
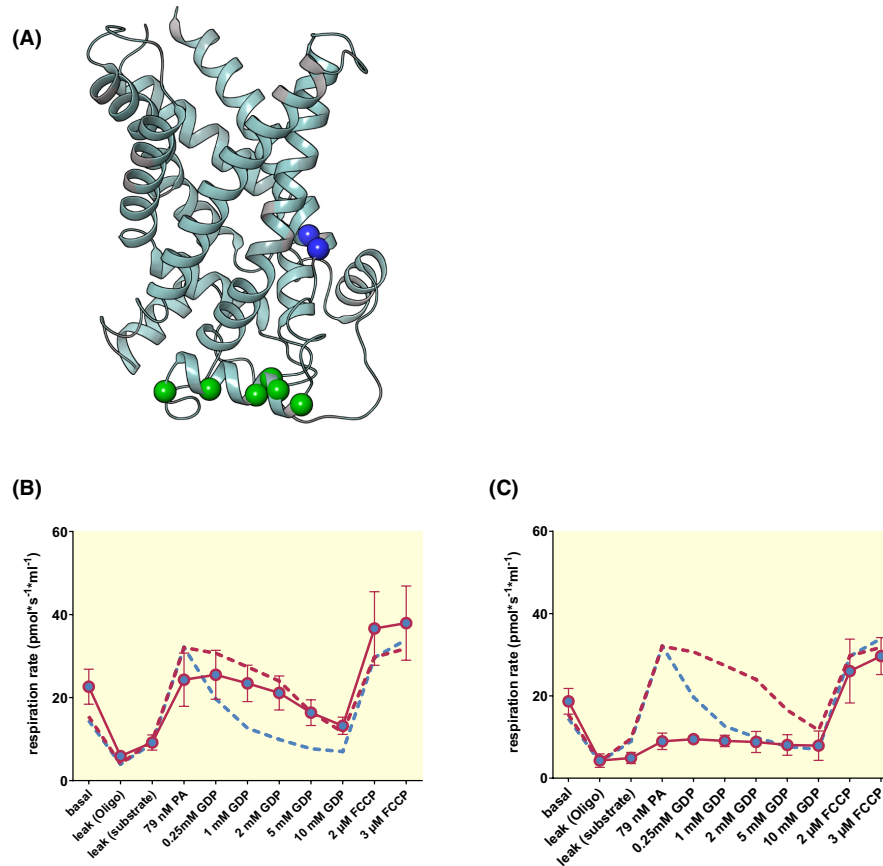
FIGURE 6 Functional consequences of building block exchanges. (A) Representation of residues in two independent building blocks in the 3D structure of UCP1. Green orbs: Residues exchanged in N-FLAG hUCP1-N-terminal-7; dark blue orbs: Residues exchanged in N-FLAG hUCP1-C-terminal-2. (B, C) Respirometry of induced HEK-293 cells expressing variant N-FLAG hUCP1 (red lines with symbols). After recording basal respiration and ATPase inhibition with oligomycin, cells were permeabilized with α-chaconine and supplied with pyruvate, malate, and succinate; UCP1 was activated through a set dose of palmitate [79 nM] followed by stepwise GDP inhibition of proton leak (0.25–10 mM). FCCP was applied to fully uncouple mitochondrial respiration. (B) Respiration rates of the N-FLAG hUCP1-N-terminal-7 variant; (C) Respiration rates of the N-FLAG hUCP1—C-terminal-2, mean $\pm$ SD, $n = 6$. Dashed lines represent the human (blue) and murine (red) wild type.

to an increase in browning in white adipose tissue but also species-specific interactions with its regulators. As hUCP1 and mUCP1 are only 79% identical, activation of proton conductance or regulation through purine nucleotides may differ. Here, we utilized a doxycycline-regulated HEK293 cell model to compare the capacity and regulation of hUCP1 and mUCP1 without tissue-specific regulatory mechanisms. This cell system will likely ensure proper protein folding and import of mammalian UCP1 into the mitochondrial inner membrane.[40] The ability to induce UCP1 expression renders non-induced cells valuable controls without the off-target biological responses of transiently or stably transfected HEK-293 cells.[41]

LCFA are natural activators of UCP1 and induce proton conductivity, thereby increasing leak respiration. The mass-specific respiratory capacity of murine and human BAT is different,[31] either due to differences in cellular heterogeneity and UCP1 concentration, species-specific differences in per-protein, fatty acid-induced UCP1 activity, or both. Here, we demonstrate that the proton leak activity of hUCP1 and mUCP1 in response to increasing LCFA concentrations is comparable when both orthologs are expressed at a similar level. Both maximal activity and dose-dependent kinetics were indistinguishable. Notably, in controls not induced to express UCP1 by doxycycline, LCFA-induced respiration was negligible at concentrations stimulating maximal proton leak respiration in UCP1-expressing cells (Figure 1E). Therefore, LCFA-induced proton leak was solely due to UCP1, excluding other mitochondrial carriers' contributions, for example, the ADP/ATP carrier, in the cell model applied. Without systemic or cell-intrinsic limitations, hUCP1 and mUCP1 can thus be assumed to feature comparable fatty-acid-induced proton leak activity within brown adipocyte mitochondria. Based on this finding, capacity estimates of

heat production in human BAT relying on UCP1 amount appear in principle justified. However, per body mass, the quantity of BAT is undoubtedly lower in humans than in rodents.

While LCFA activate UCP1, purine nucleotides negatively regulate activity. Under basal conditions, UCP1 occurs in a purine nucleotide-bound c-state-like conformation, rendering it inactive.[20] A beta-adrenergic stimulus releases free fatty acids from intracellular lipid droplets and overcomes purine nucleotide inhibition. At the same time, purine nucleotide concentrations drop by degradation and cation complexation.[38] Here, we tested the regulative capacities of the purine nucleotides ADP and GDP on hUCP1 and mUCP1. While ADP is the physiologically more abundant purine nucleotide, most studies employed GDP for UCP1 inhibition, in part for the historical background of UCP1 being initially described as a GDP-binding protein, but also to avoid interference of ADP (or ATP) with the ADP/ATP carrier and the ATP-synthase.

The comparison of hUCP1 and mUCP1 regulation by ADP versus GDP is vital as the exact cellular abundances may differ in rodent and human brown and beige adipocytes (e.g., fivefold more ADP than GDP in HEK cells, 2.5-fold in primary brown adipocytes).[38] We found that ADP is equally potent in inhibiting hUCP1 and mUCP1, and equivalent concentrations of LFCA are required to counteract this inhibitory effect. This implies that the equal activation by LCFA is not secondary to stronger binding affinities of the protein for ADP.

Despite equal regulation by LCFA and ADP, we found that hUCP1 shows a reduced sensitivity toward GDP than mUCP1. This finding relies on our experimental data, which show that the activity of the FLAG-tagged UCP1 is not altered but should be corroborated by testing either the wild-type UCP1 and UCP1 constructs FLAG-tagged with a linker sequence. In support of our findings, however, GDP was also less potent in inhibiting palmitate-stimulated respiration of wild-type hUCP1 compared to mUCP1 and rat UCP1 in a yeast expression system.[30] Respiration measurements did detect GDP sensitivity of human BAT, although the dose responses were not titrated.[31] In our hands, the physiologically important ADP sensitivity is conserved in both UCP1 orthologs. Based on this finding, using ADP instead of GDP for mitochondrial or cellular respirometry experiments appears vital to transferring conclusions drawn from rodent models to humans.

So far, hypotheses on the mechanism of UCP1-dependent proton leak have referred mainly to the structure–function relationships in other mitochondrial carriers, particularly the ADP/ATP carrier.[5] The recent provision of hUCP1 structures has delivered novel insights into how purine nucleotides inhibit proton conductance catalyzed by UCP1.[20,21] Consequently, the structural information will be instrumental in elucidating how LCFA override purine nucleotide inhibition. The functional competition of LCFA and purine nucleotides in regulating UCP1-dependent proton leak has been known for decades,[6] but they most likely do not compete for the same binding site.[25,42–45] Under physiological conditions, nucleotides are always bound to UCP1, resulting in a closed matrix gate of the protein. As suggested based on the new structural data, the binding of LCFA to hydrophobic residues in the central cavity may initiate state transitions, akin to transport substrates of other carriers, as part of the mechanism.[20]

The results of our study are compatible with this proposed mechanism. To identify amino acids involved in the differential GDP sensitivity of hUCP1 and mUCP1, we found two structural building blocks to be essential for hUCP1 activity: the small α-helix located in the loop between transmembrane α-helix 5 and 6 and two amino acids at the N-terminus of transmembrane α-helix 6. Three individual amino acid exchanges in α-helix 56 rendered hUCP1 less active, as suggested by significant differences observed in curve fitting for EC50 and maximal respiration, but the individual contribution of the two parameters was not discernible (Table S5; Figure S5). However, the difference was not observed when exchanging the entire α-helix 56 building block (see N-terminal-7). Arranged parallel to the membrane, these residues contribute to the matrix insulator area and the matrix salt bridge network, closing the central cavity of UCP1, thereby blocking proton leak in the nucleotide-bound state.[20,21] We hypothesize that by exchanging individual amino acids of these essential building blocks, we altered the matrix salt bridge network, stabilizing the c-state in hUCP1 mutants. The binding of LCFA to these mutants cannot overcome proton conductance inhibition. These findings demonstrate that amino acids in α-helix 56 are critical for hUCP1 function.

The effect of individual amino acid exchanges on the small α-helix 56 was fully compensated by inserting the complete mouse amino acids. Conversely, a single exchange of L271 and P273 at the beginning of the α-helix 6 and the combination of both resulted in a non-functional protein and did not compensate for each other. The hydrophobic L271 interacts with cardiolipin in the UCP1 structure (PDB ID: 8G8W).[20] Cardiolipin was found to be essential for UCP1 stability[14] and binds in proximity to the beginning of α-helix 6 for the ADP/ATP carrier.[17] Notably, the loss-of-function substitution replaces a proline residue, predominant in eutherian mammals at this position[46] and most likely plays a crucial role in UCP1 function. In general, proline is known for the unique rigidity it introduces into a protein structure. Furthermore, proline is known to form

weak points at the beginning of α-helices. These weak points are believed to facilitate the transmembrane channel movements necessary for their function.[47,48] It is, therefore, likely that the P273 residue in hUCP1 stabilizes a kink conformation that serves the purpose of a hinge in hUCP1, thus allowing the protein to transition from the c-state to the m-state. The fatal effect of P273A implies the necessity of conformational stability at this hinge position critical for hUCP1 activation. Intriguingly, mUCP1 is exceptional in having an alanine residue at this position, though mUCP1 is certainly fully functional. The loss of proline in mUCP1 appears to have been compensated by subsequent tertiary contacts stabilizing the kink conformation.[49]

We aimed to determine whether hUCP1 and mUCP1 have similar activity and capacity and whether the knowledge gained from rodent studies can be applied to hUCP1. Only then can assumptions regularly made in efficacy estimates of putative drugs intended to target this protein in the context of human metabolic disease be drawn. Here, we demonstrate that hUCP1 and mUCP1 activation by LCFA and the regulatory properties of ADP are comparable. Based on this, capacity estimates based on the UCP1 amount seem justified. Furthermore, we show that hUCP1 is significantly less sensitive to GDP inhibition than the murine ortholog. However, the physiological relevance of this finding is debatable due to the far lower cytosolic abundance of GDP compared to ADP. We suggest that conserved sensitivity instead places ADP at the pole position as the most physiologically relevant modulator of UCP1 activity. Introducing nine murine amino acid residues into the hUCP1 did not confer high GDP sensitivity to hUCP1. In the process, we discovered that α-helix 56 and the amino acids L271 and P273 at the N-terminus of α-helix 6 are essential for hUCP1 activity. The disruption of the two structural components renders UCP1 ineffective in humans. We hypothesize that both building blocks play an essential role in the conformational change induced by the binding of LCFA, which destabilizes the c-state and results in the opening of the matrix gate. The absence of L271 and P273 cannot be compensated for in hUCP1. While we could not conclusively clarify the different GDP sensitivities between orthologs or explain the variation through our functional model, it is plausible that L271 and P273 contribute to the variable GDP sensitivity of hUCP1 and mUCP1.

4 | MATERIALS AND METHODS

4.1 | Cell culture

HEK-293 cells (Flp-In™-T-REx™) were routinely cultured in Dulbecco's Modified Eagle Medium (4500 mg/L glucose, L-glutamine, and sodium bicarbonate, Sigma-Aldrich D5796) supplemented with 10% fetal bovine serum (Sigma-Aldrich S0615), 20 μg/mL Gentamycin, 150 μg/mL Hygromycin and 5 μg/mL Blasticidin at 37°C and 5% CO_2 in a humidified incubator.

The generation of Flp-In™-T-REx™ expression in HEK-293 cell lines was performed according to the manufacturer. In short, the full-length coding sequence of human (NM_021833.5) and murine (NM_009463) UCP1 was cloned into pcDNA5.1 (Invitrogen). The coding sequences were FLAG-tagged either at the N- or C-terminus. Calcium-phosphate-mediated co-transfection with pcDNA5.1 and pOG44 in Flp-In™-T-REx™ cells was performed at 50%–60% confluency, and positive clones were selected by hygromycin treatment for 2 weeks. Single clonal cell colonies were picked, grown separately, and verified by sequencing (Eurofins Genomics). To induce UCP1 expression, HEK-293 cells were seeded on a 10-cm petri dish in a medium containing 2.5 ng/mL doxycycline for 3 days with daily medium change.

Cell growth was monitored by continuous live cell imaging (Incucyte® System, Sartorius). On the day of the experiment, 0.3×10^6 cells were seeded into 6-well plates. Control cells were cultured in a routine culture medium, and induced cells were cultured in a doxycycline-containing medium (2.5 ng/mL), with daily medium changes. Cell growth was recorded for 72 h.

4.2 | Localization of ectopically expressed UCP1

HEK-293 cells were seeded and induced as described above. On the second induction day, cells were transferred from the 10-cm petri dish to a 35 mm μ-dish with a seeding density of 0.3×10^6 cells. On the third day, cells were fixed: Medium was aspirated, and the cells were washed with PBS. The cells were incubated for 1 h at 4°C with buffered formalin (29 mM $NaH_2PO_4 \times H_2O$ (Sigma-Aldrich, S–9638), 56.3 mM $Na_2HPO_4 \times 7H_2O$ (Sigma-Aldrich, S-9390), 3.7% Formaldehyde solution (Sigma-Aldrich F-1635)) and washed three times for 10 min with PBS. Cells were preincubated with 200 μL PBS azide solution (PBS supplemented with 4% horse serum, 0.5% Triton X, and 15.4 mM NaN3) at room temperature for immune cytochemistry. First antibodies (Anti-DYKDDDDK Tag Polyclonal Antibody (Invitrogen) and HSP60 Monoclonal Antibody (Proteintech) were applied overnight at room temperature. Before the application of the secondary antibodies (Anti-Rabbit IgG (H + L) Highly cross-absorbed, Alexa Fluor™ 546 (Invitrogen), Goat anti-Mouse IgG (H + L) Cross-Adsorbed Secondary

Antibody, Alexa Fluor™ 647 (Invitrogen)) for 2 h at room temperature, cells were washed three times 10 min with PBS. Before the application of the mounting medium (Fluoroshield™ with DAPI, Sigma-Aldrich), the washing steps were repeated.

4.3 | Functional characterization through respirometry

Clarke-type respirometry measurements were performed using the OROBOROS Oxygraph-2k and recorded by the software DatLab 4 (OROBOROS Instruments, Innsbruck, Austria). Cells were harvested and resuspended in mitochondrial respiration buffer (0.5 mM EGTA, 3 mM $MgCl_2 \times 6 H_2O$, 60 mM lactobionic acid, 20 mM taurine, 10 mM KH_2PO_4, 20 mM HEPES, 110 mM D-sucrose, 1 g/L BSA essentially fatty acid-free). Cell amount was determined via Biorad Automated Cell Counter (TC20, Biorad) and 1.0×10^6 cells per measurement were transferred into the air-calibrated Mir05-containing chambers of the Oxygraph-2k. For fatty acid titration, the following substrate-uncoupling-inhibitor protocol was used: after recording basal respiration, the ATPase inhibitor oligomycin (2 mg/mL) was added to determine leak respiration; 15 μM α-chaconine (Extrasynthese 1553 S) resulted in membrane permeabilization, followed by 5 mM pyruvate, 2 mM malate and 5 mM succinate to energize OXPHOS; subsequently, BSA/FA mixtures with different ratios were added until maximal FA-induced leak respiration was reached; 1 mM GDP was applied to ensure the functionality of UCP1; the complex III inhibitor Antimycin A (2.5 μg/mL) followed to inhibit electron flow.

For purine nucleotide titration the following substrate-uncoupling-inhibitor protocol was used: After recording basal respiration, the ATPase inhibitor oligomycin (2 mg/mL) was added to determine leak respiration; 15 μM α-chaconine (Extrasynthese 1553 S) resulted in membrane permeabilization,[50] followed by 5 mM pyruvate, 2 mM malate, and 5 mM succinate to energize OXPHOS; to activate UCP1 a BSA/PA bolus was added (ratio 1:25, free fatty acid concentration: 79 nM); subsequently, GDP/ADP was titrated (0.25, 1, 2, 5, 10 mM). FCCP was titrated up to 4 μM, and finally, the complex III inhibitor Antimycin A (2.5 μg/mL) followed to inhibit electron flow.

Palmitic/oleic acid solutions complexed with BSA (essentially fatty acid-free, Sigma-Aldrich A3803) were freshly made on the measurement day. For the preparation, fatty acids (200 mM in 70% EtOH) were solved in different ratios in Mir05 containing 10% BSA (essentially fatty acid-free, Sigma-Aldrich A3803). The free fatty acid concentration was calculated as described previously.[51] Solutions were incubated for 1.5 h at 37°.

4.4 | Quantification of glucose uptake

HEK-293 cells were induced for 2 days. On the third day, induced cells were trypsinized, and 0.3×106 cells were seeded into 6-well plates and cultured overnight with a routine culture medium. On the day of the measurement, the medium was replaced with fresh induction medium, routine culture medium, or induction medium enriched with free fatty acids (DMEM, 20 μg/mL gentamycin, 1% essentially fatty acid-free BSA, 0.8 mM oleic acid, 0.4 mM palmitic acid). One sample of each condition (time point 0) was taken. Cells were incubated at 37°C in a 5% CO_2 humidified incubator. After 3 and 24 h, samples were taken. Glucose concentrations were determined using a blood glucose-measuring device (FreeStyle Freedom Lite). The sample was mixed with 100% glycerol in a 6:4 ratio to ensure proper viscosity. One drop per sample was applied to the test stripes. Each sample was measured in triplicate.

4.5 | Mutagenesis

We performed site-directed mutagenesis, creating HEK-293 N-FLAG mUCP1 mutants according to the kit protocol (QuikChange Lightning, Agilent). Primers were generated using QuikChange Primer Design from Agilent (Table S1). Two silent point mutations were introduced to get two new single-cutting restriction sites (Table S2). We then constructed two oligonucleotide pairs; one contained the first seven mutations (P244L, K249P, N253S, K257S, V258M, F259Y, and N261K) on the α-helix 56 (fragment 1). The second oligonucleotide pair contained the mutations L271F and P273A (fragment 2; Table S3). Annealed oligonucleotides were cloned into pcDNA5.1-hUCP1 vector digested with the respective restriction enzymes (SgrAI + PpuMI = fragment 1; PpuMI + BamHI = fragment 2) for 1 h at 37°C. Restriction enzymes were inactivated at 75°C for 5 min and digested vector and annealed oligonucleotides ligated in a 1:6 ratio.

4.6 | Western blotting and UCP1 standard

A recombinant N-FLAG mUCP1 standard was produced in E. coli KS272 using a pASK75-His-mUCP1-Flag plasmid. After cell disruption, the insoluble protein fraction was washed three times with PBS containing 0.1% Tween, dissolved in 2.5 M GdmCl, and the soluble fraction was purified by size exclusion chromatography using a Superdex S75 Prep Grade column (Cytvia—17104402). Protein concentration and purity of the standard were

determined through an SDS polyacrylamide gel and subsequent Coomassie staining. Coomassie staining was quantified through the Odyssey scanner (LI-COR system). Protein concentration was calculated using BSA samples with known concentrations. To determine the purity of the UCP1 standard, the recombinant UCP1 band intensity was normalized to the total signal intensity of the gel lane. The protein of each respirometry sample was extracted using RIPA buffer (50 mM Tris-Cl), 1% (v/v) NP-40, 0.25% (w/v) Na-deoxycholate, 150 mM NaCl, 1 mM EDTA, 1:1000 protease inhibitor (P8340, Sigma-Aldrich), 1:1000 phosphatase inhibitor (P5726, Sigma-Aldrich). Protein concentration was determined using a bicinchoninic acid assay (PierceTM BCA Assay Kits, Thermo Scientific). Equal amounts of samples (25 μg protein) and different concentrations of the recombinant mUCP1 standard (10, 5, 2.5, 1.25 ng) were loaded on a 12.5% SDS-PAGE gel and blotted onto a nitrocellulose membrane. After blocking in Tris-buffered saline (TBS) containing 2% (w/v) bovine serum albumin overnight, the membrane was incubated with primary antibodies, including rabbit anti-FLAG (Invitrogen), and mouse anti-actin (Millipore MAB1501) for 1.5 h at room temperature.

Before incubating with the secondary antibodies IRDye® 800CW goat anti-rabbit and IRDye® 680CW donkey anti-mouse for 1.5 h at room temperature, membranes were washed three times for 5 min with TBS + 0.1% Tween20. The washing steps were repeated after the incubation with the second antibody. The Odyssey Infrared Imaging System detected fluorescence signal intensity (LI-COR). The signal was quantified using Image StudioTM Lite Software (LI-COR). Based on the signal intensities of recombinant mUCP1, a standard curve was calculated, and the UCP1 concentration per HRR sample was determined.

4.7 | Statistical analyses

Data are presented as mean values ± standard deviation unless stated otherwise. All analyses have been performed with GraphPad Prism. Dose–response curves were calculated through a least square regression assuming a four-parameter sigmoidal relationship to log[compound] (i.e., palmitate or GDP) with a fixed bottom respiration value. A comparison of fitted models was performed using an extra sum-of-square F test, including the parameter(s) to compare (half maximal dose, maximal respiration rate). Multiple group comparisons were performed using Tukey's multiple comparison test. For EC50 values of palmitate-induced respiration, we also fitted single replicate curves with maximal respiration set to 100%, modeled with fixed bottom and top. p-values < 0.05 were considered significant. $N = 1$ represents one measurement of the exact cellular clone but in consecutive measurements.

4.8 | Structural model of human UCP1

The 3D structure of UCP1 in complex with GTP was downloaded from the Protein Data Bank (PDB ID: 8G8W). Using the Protein Preparation Wizard workflow available in Maestro (Schrödinger Release 2022-3, Maestro, Schrödinger, LLC, New York, NY, 2022), hydrogens and missing side chains were added to the protein. We removed the Pro-microbodies 65 and 71 and minimized the structure to a derivative convergence of 0.05 kJ/mol-Å using the Polak–Ribiere Conjugate Gradient (PRCG) minimization algorithm, the OPLS2005 force field, and the GB/SA water solvation model implemented in MacroModel (Schrödinger Release 2022-3, Maestro, Schrödinger, LLC, New York, NY, 2022). We used Maestro to visualize the amino acids of H56 and H6 and prepare a structural representation. Ethics approval for the experiments conducted in the present study was not required.

AUTHOR CONTRIBUTIONS

Eva Musiol: Data curation; formal analysis; visualization; writing – original draft; methodology; investigation. **Tobias Fromme:** Data curation; formal analysis; writing – original draft; conceptualization; methodology; supervision; writing – review and editing. **Julia Hau:** Visualization; methodology; investigation. **Antonella Di Pizio:** Formal analysis; visualization; writing – review and editing; supervision; methodology; software. **Martin Klingenspor:** Conceptualization; data curation; formal analysis; visualization; writing – original draft; writing – review and editing; project administration; supervision; funding acquisition; validation; methodology.

CONFLICT OF INTEREST STATEMENT

The corresponding author declares that there is no conflict of interest.

DATA AVAILABILITY STATEMENT

ORCID

Tobias Fromme https://orcid.org/0000-0001-9150-2513
Antonella Di Pizio https://orcid.org/0000-0002-8520-5165
Martin Klingenspor https://orcid.org/0000-0002-4502-6664

REFERENCES

1. Cypess AM, Lehman S, Williams G, et al. Identification and importance of brown adipose tissue in adult humans. *N Engl J Med*. 2009;360(15):1509-1517.
2. van Marken Lichtenbelt WD, Vanhommerig JW, Smulders NM, et al. Cold-activated brown adipose tissue in healthy men. *N Engl J Med*. 2009;360(15):1500-1508.
3. Virtanen KA, Lidell ME, Orava J, et al. Functional brown adipose tissue in healthy adults. *N Engl J Med*. 2009;360(15):1518-1525.
4. Becher T, Palanisamy S, Kramer DJ, et al. Brown adipose tissue is associated with cardiometabolic health. *Nat Med*. 2021;27(1):58-65.
5. Crichton PG, Lee Y, Kunji ERS. The molecular features of uncoupling protein 1 support a conventional mitochondrial carrier-like mechanism. *Biochimie*. 2017;134:35-50.
6. Nicholls DG. A history of UCP1. *Biochem Soc Trans*. 2001;29(Pt 6):751-755.
7. Cannon B, Nedergaard J. Brown adipose tissue: function and physiological significance. *Physiol Rev*. 2004;84(1):277-359.
8. Rial E, González-Barroso MM. Physiological regulation of the transport activity in the uncoupling proteins UCP1 and UCP2. *Biochim Biophys Acta*. 2001;1504(1):70-81.
9. Winkler E, Klingenberg M. Effect of fatty acids on H+ transport activity of the reconstituted uncoupling protein. *J Biol Chem*. 1994;269(4):2508-2515.
10. Garlid KD, Orosz DE, Modriansky M, Vassanelli S, Jezek P. On the mechanism of fatty acid-induced proton transport by mitochondrial uncoupling protein. *J Biol Chem*. 1996;271(5):2615-2620.
11. Fedorenko A, Lishko PV, Kirichok Y. Mechanism of fatty-acid-dependent UCP1 uncoupling in brown fat mitochondria. *Cell*. 2012;151(2):400-413.
12. Robinson AJ, Kunji ERS. Mitochondrial carriers in the cytoplasmic state have a common substrate binding site. *Proc Natl Acad Sci USA*. 2006;103(8):2617-2622.
13. Kunji ERS, Crichton PG. Mitochondrial carriers function as monomers. *Biochim Biophys Acta*. 2010;1797(6–7):817-831.
14. Lee Y, Willers C, Kunji ERS, Crichton PG. Uncoupling protein 1 binds one nucleotide per monomer and is stabilized by tightly bound cardiolipin. *Proc Natl Acad Sci USA*. 2015;112(22):6973-6978.
15. Pebay-Peyroula E, Dahout-Gonzalez C, Kahn R, Trézéguet V, Lauquin GJ-M, Brandolin G. Structure of mitochondrial ADP/ATP carrier in complex with carboxyatractyloside. *Nature*. 2003;426(6962):39-44.
16. Ruprecht JJ, Hellawell AM, Harding M, Crichton PG, McCoy AJ, Kunji ERS. Structures of yeast mitochondrial ADP/ATP carriers support a domain-based alternating-access transport mechanism. *Proc Natl Acad Sci USA*. 2014;111(4):E426-E434.
17. Ruprecht JJ, King MS, Zögg T, et al. The molecular mechanism of transport by the mitochondrial ADP/ATP carrier. *Cell*. 2019;176(3):435-447.e15.
18. Walker JE, Runswick MJ. The mitochondrial transport protein superfamily. *J Bioenerg Biomembr*. 1993;25(5):435-446.
19. Nelson DR, Felix CM, Swanson JM. Highly conserved charge-pair networks in the mitochondrial carrier family. *J Mol Biol*. 1998;277(2):285-308.
20. Jones SA, Gogoi P, Ruprecht JJ, et al. Structural basis of purine nucleotide inhibition of human uncoupling protein 1. *Sci Adv*. 2023;9(22):eadh4251.
21. Kang Y, Chen L. Structural basis for the binding of DNP and purine nucleotides onto UCP1. *Nature*. 2023;620(7972):226-231.
22. Mayinger P, Klingenberg M. Labeling of two different regions of the nucleotide binding site of the uncoupling protein from brown adipose tissue mitochondria with two ATP analogs. *Biochemistry*. 1992;31(43):10536-10543.
23. Winkler E, Klingenberg M. Photoaffinity labeling of the nucleotide-binding site of the uncoupling protein from hamster brown adipose tissue. *Eur J Biochem*. 1992;203(1–2):295-304.
24. González-Barroso MM, Fleury C, Levi-Meyrueis C, Zaragoza P, Bouillaud F, Rial E. Deletion of amino acids 261-269 in the brown fat uncoupling protein converts the carrier into a pore. *Biochemistry*. 1997;36(36):10930-10935.
25. Modriansky M, Murdza-Inglis DL, Patel HV, Freeman KB, Garlid KD. Identification by site-directed mutagenesis of three arginines in uncoupling protein that are essential for nucleotide binding and inhibition. *J Biol Chem*. 1997;272(40):24759-24762.
26. Echtay KS, Bienengraeber M, Klingenberg M. Mutagenesis of the uncoupling protein of brown adipose tissue. Neutralization of E190 largely abolishes pH control of nucleotide binding. *Biochemistry*. 1997;36(27):8253-8260.
27. Gagelin A, Largeau C, Masscheleyn S, et al. Molecular determinants of inhibition of UCP1-mediated respiratory uncoupling. *Nat Commun*. 2023;14(1):2594.
28. Hirschberg V, Fromme T, Klingenspor M. Test systems to study the structure and function of uncoupling protein 1: a critical overview. *Front Endocrinol (Lausanne)*. 2011;2:63.
29. Beck V, Jabůrek M, Breen EP, Porter RK, Jezek P, Pohl EE. A new automated technique for the reconstitution of hydrophobic proteins into planar bilayer membranes. Studies of human recombinant uncoupling protein 1. *Biochim Biophys Acta*. 2006;1757(5–6):474-479.
30. Rodríguez-Sánchez L, Rial E. The distinct bioenergetic properties of the human UCP1. *Biochimie*. 2017;134:51-55.
31. Porter C, Herndon DN, Chondronikola M, et al. Human and mouse Brown adipose tissue mitochondria have comparable UCP1 function. *Cell Metab*. 2016;24(2):246-255.

32. Trayhurn P. Origins and early development of the concept that brown adipose tissue thermogenesis is linked to energy balance and obesity. *Biochimie*. 2017;134:62-70.

33. Geisler JG. Targeting energy expenditure via fuel switching and beyond. *Diabetologia*. 2011;54(2):237-244.

34. Townsend KL, Tseng Y-H. Of mice and men: novel insights regarding constitutive and recruitable brown adipocytes. *Int J Obes Suppl*. 2015;5(Suppl 1):S15-S20.

35. Ahler E, Sullivan WJ, Cass A, et al. Doxycycline alters metabolism and proliferation of human cell lines. *PLoS One*. 2013;8(5):e64561.

36. O'Gorman S, Fox DT, Wahl GM. Recombinase-mediated gene activation and site-specific integration in mammalian cells. *Science*. 1991;251(4999):1351-1355.

37. Lin CS, Klingenberg M. Characteristics of the isolated purine nucleotide binding protein from brown fat mitochondria. *Biochemistry*. 1982;21(12):2950-2956.

38. Fromme T, Kleigrewe K, Dunkel A, et al. Degradation of brown adipocyte purine nucleotides regulates uncoupling protein 1 activity. *Mol Metab*. 2018;8:77-85.

39. Scheele C, Nielsen S. Metabolic regulation and the anti-obesity perspectives of human brown fat. *Redox Biol*. 2017;12:770-775.

40. Jastroch M, Hirschberg V, Klingenspor M. Functional characterization of UCP1 in mammalian HEK293 cells excludes mitochondrial uncoupling artefacts and reveals no contribution to basal proton leak. *Biochim Biophys Acta*. 2012;1817(9):1660-1670.

41. Jacobsen L, Calvin S, Lobenhofer E. Transcriptional effects of transfection: the potential for misinterpretation of gene expression data generated from transiently transfected cells. *BioTechniques*. 2009;47(1):617-624.

42. Echtay KS, Winkler E, Bienengraeber M, Klingenberg M. Site-directed mutagenesis identifies residues in uncoupling protein (UCP1) involved in three different functions. *Biochemistry*. 2000;39(12):3311-3317.

43. Klingenberg M. Uncoupling proteins–how do they work and how are they regulated. *IUBMB Life*. 2001;52(3–5):175-179.

44. Shabalina IG, Jacobsson A, Cannon B, Nedergaard J. Native UCP1 displays simple competitive kinetics between the regulators purine nucleotides and fatty acids. *J Biol Chem*. 2004;279(37):38236-38248.

45. Divakaruni AS, Humphrey DM, Brand MD. Fatty acids change the conformation of uncoupling protein 1 (UCP1). *J Biol Chem*. 2012;287(44):36845-36853.

46. Gaudry MJ, Jastroch M. Molecular evolution of uncoupling proteins and implications for brain function. *Neurosci Lett*. 2019;696:140-145.

47. Tieleman DP, Shrivastava IH, Ulmschneider MR, Sansom MS. Proline-induced hinges in transmembrane helices: possible roles in ion channel gating. *Proteins*. 2001;44(2):63-72.

48. Jin T, Peng L, Mirshahi T, et al. The (beta)gamma subunits of G proteins gate a K(+) channel by pivoted bending of a transmembrane segment. *Mol Cell*. 2002;10(3):469-481.

49. Yohannan S, Faham S, Yang D, Whitelegge JP, Bowie JU. The evolution of transmembrane helix kinks and the structural diversity of G protein-coupled receptors. *Proc Natl Acad Sci USA*. 2004;101(4):959-963.

50. Dawid C, Weber D, Musiol E, et al. Comparative assessment of purified saponins as permeabilization agents during respirometry. *Biochim Biophys Acta Bioenerg*. 2020;1861(10):148251.

51. Richieri GV, Anel A, Kleinfeld AM. Interactions of long-chain fatty acids and albumin: determination of free fatty acid levels using the fluorescent probe ADIFAB. *Biochemistry*. 1993;32(29):7574-7580.

SUPPORTING INFORMATION

Additional supporting information can be found online in the Supporting Information section at the end of this article.